nature photonics

Article

https://doi.org/10.1038/s41566-024-01491-2

Bose–Einstein condensation of light in a semiconductor quantum well microcavity

Received: 10 August 2023

Accepted: 28 June 2024

Published online: 12 August 2024

Check for updates

Ross C. Schofield[1] ✉, Ming Fu[1], Edmund Clarke[2], Ian Farrer[2], Aristotelis Trapalis[2], Himadri S. Dhar[3], Rick Mukherjee[1,4], Toby Severs Millard[1], Jon Heffernan[2], Florian Mintert[1,5], Robert A. Nyman[1] & Rupert F. Oulton[1] ✉

When particles with integer spin accumulate at low temperature and high density, they undergo Bose–Einstein condensation (BEC). Atoms, magnons, solid-state excitons, surface plasmon polaritons and excitons coupled to light exhibit BEC, which results in high coherence due to massive occupation of the respective system's ground state. Surprisingly, photons were shown to exhibit BEC recently in organic-dye-filled optical microcavities, which—owing to the photon's low mass—occurs at room temperature. Here we demonstrate that photons within an inorganic semiconductor microcavity also thermalize and undergo BEC. Although semiconductor lasers are understood to operate out of thermal equilibrium, we identify a region of good thermalization in our system where we can clearly distinguish laser action from BEC. Semiconductor microcavities are a robust system for exploring the physics and applications of quantum statistical photon condensates. In practical terms, photon BECs offer their critical behaviour at lower thresholds than lasers. Our study shows two further advantages: the lack of dark electronic states in inorganic semiconductors allows these BECs to be sustained continuously; and quantum wells offer stronger photon–photon scattering. We measure an unoptimized interaction parameter ($\tilde{g} \gtrsim 10^{-3}$), which is large enough to access the rich physics of interactions within BECs, such as superfluid light.

Semiconductor lasers, first realized in the 1960s[1,2], are now an essential underpinning technology, ubiquitous in research and industry due to their ability to generate bright, coherent and directional radiation from electricity. A conventional understanding of the laser process in a semiconductor involves a population inversion of electrons, excited from the valence band to the conduction band, which amplifies its own light emission within an optical resonator. The apparently extreme conditions necessary for optical gain suggest that neither the semiconductor's electrons nor resonant photons can be in thermal equilibrium, either with themselves or each other. Despite this intuition, however, steady-state optical gain in semiconductors arises from electrons and holes in quasi-thermal equilibrium[3]. Furthermore, it is well known that a detailed balance of absorption and emission allows electromagnetic radiation to be in thermal equilibrium with its surroundings. Under ambient conditions, Planck's spectrum peaks in the mid-infrared while visible and near-infrared light may also achieve thermal equilibrium when interacting with suitable light emission materials[4,5]. This has been demonstrated for organic dye embedded in and tuned to an optical cavity resonator with a well-defined ground state[6]. In this system, with increasing excitation, the photon population reaches a critical

[1]Blackett Laboratory, Imperial College London, London, UK. [2]EPSRC National Epitaxy Facility, University of Sheffield, Sheffield, UK. [3]Department of Physics, Indian Institute of Technology Bombay, Mumbai, India. [4]Center for Optical Quantum Technologies, Department of Physics, University of Hamburg, Hamburg, Germany. [5]Helmholtz-Zentrum Dresden-Rossendorf, Dresden, Germany. ✉e-mail: ross.schofield@imperial.ac.uk; r.oulton@imperial.ac.uk

https://doi.org/10.1038/s41566-024-01491-2

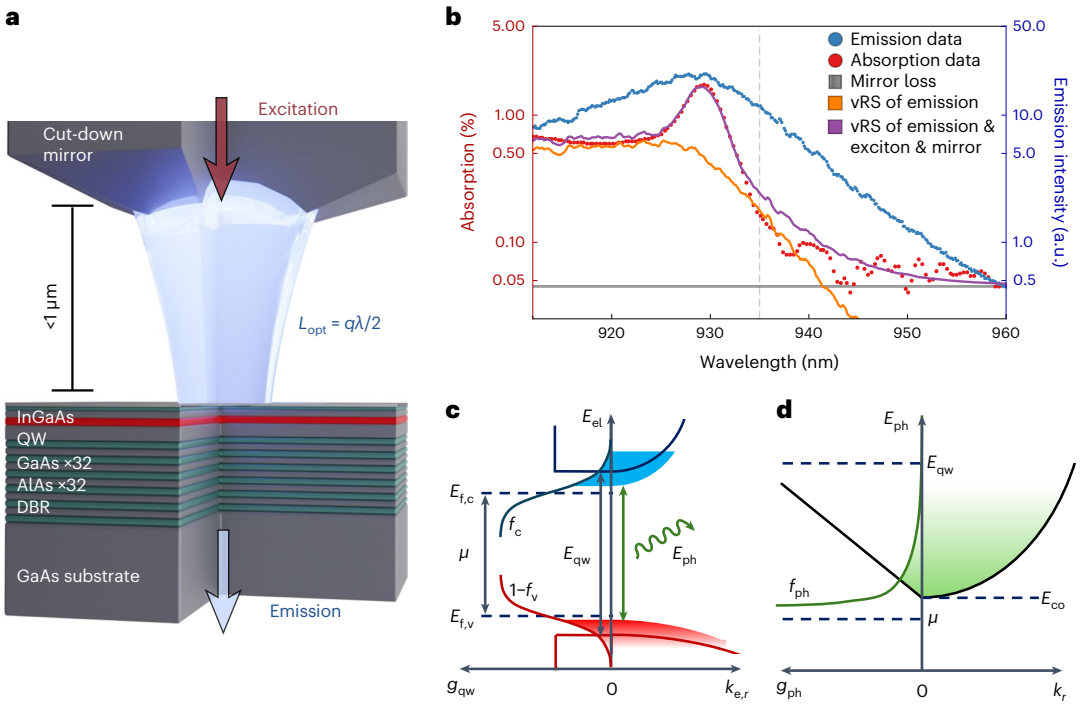

Fig. 1 | Device structure and quantum well spectral information. a, Illustration of the inorganic semiconductor quantum well microcavity. **b**, Quantum well emission spectrum (blue points) and absorption spectrum (red points). The vRS relation transforms the photoluminescence spectrum into the naïvely expected absorption spectrum (orange line) for a semiconductor in thermal equilibrium. Accounting for the mirror loss (grey line) and bound exciton absorption at 930 nm gives good correspondence between the predicted (purple line) and measured (red points) absorption spectrum. We expect thermalization to occur to the right of the dashed vertical line, where absorption and emission follow the vRS relation and the mirrors have high reflectivity. **c**, Electronic dispersion and thermal population densities following Fermi–Dirac statistics. **d**, Photon dispersion and thermal population density following Bose–Einstein statistics.

number where the chemical potential of light approaches the cavity's ground-state energy and Bose–Einstein condensation (BEC) occurs[7]. BEC has been observed in a wide range of boson systems, including atoms[8,9], magnons[10], solid-state excitons[11], surface plasmon polaritons[12] and excitons coupled to light[13]. Although offering the high temporal and spatial coherence characteristics of lasers, condensates of light are distinct as they robustly operate in their ground state, exhibit nonlinear and many-body physics described by quantum statistical mechanics and do not require carrier inversion, because of which they manifest critical behaviour below the laser threshold[13,14].

In this work, we identify the operating regime of inorganic semiconductor microcavities where their electronic and photonic populations are in thermal equilibrium and thus produce condensates of light at room temperature. Excited using a continuous-wave laser, these condensates can be indefinitely sustained, something that was achieved even for matter-based condensates only recently[15]. We study the photon condensate as a function of the light–matter coupling strength, allowing us to identify the phases of lasing and condensation, which closely follow theoretical predictions[16]. This establishes the underpinning physics of photon condensation in inorganic semiconductor microcavities, confirming evidence of this interpretation in related vertical-cavity surface-emitting lasers[17] and other semiconductor systems[18]. This is also supported by other recent works developing the theory of BEC in semiconductor cavities[19,20].

Our approach brings key advantages compared with other optical condensates. Inorganic semiconductor materials have much lower transition rates from bright to long-lived dark states than those of organic dyes, which avoids the requirement for low-repetition-rate pulsed excitation to avoid the shelving of carriers[7]. Distinct from the condensation of exciton-cavity polaritons[13,18,21,22], condensates of light are only weakly coupled to their surroundings and therefore bypass the low temperatures and limited excitation conditions often necessary to sustain bound excitons. Even for materials with stable excitons at room temperature, condensed polaritons dissociate under strong excitation, where they revert to normal laser operation[18,23,24]. These advantages enable the use of technically relevant III–V materials as an environment for exploring the physics and application of quantum statistical condensates despite their low exciton binding energies.

Figure 1a illustrates the inorganic semiconductor microcavity. One half is a GaAs/AlAs heterostructure distributed Bragg reflector (DBR) and InGaAs quantum well, whereas the other half is a commercially manufactured DBR on a concave glass substrate with a radius of curvature of $\rho = 0.2$ m (Fig. 1b and Methods). The use of two separate mirrors allows an independent characterization of the quantum well and cavity length control. The cavity length $\bar{L}$ was locked in position with interferometric stabilization (Methods). All the measurements were performed with a longitudinal mode number of $q = 9$ to ensure that the quantum well emits into a single longitudinal mode. The commercial mirror has reflectivity $R_b > 99.995\%$, whereas the semiconductor mirror has reflectivity $R_f > 99.950\%$; therefore, light is mainly emitted through the GaAs substrate. The cavity loss rate, $\kappa_{q=9} = 1.6 \pm 0.2 \times 10^{10}\ s^{-1}$, was estimated from the laser threshold and reflection measurements (Supplementary Information), and is consistent with the mirror reflectivities, which give $\kappa > 10^{10}\ s^{-1}$.

The microcavity defines a two-dimensional photon mode spectrum:

$$E_{ph}(k_r, r) = \frac{mc^2}{n^2} + \frac{\hbar^2 k_r^2}{2m} + \frac{1}{2}m\Omega^2 r^2 - mc^2\frac{n_2}{n^3}I(r), \qquad (1)$$

which is a function of axial position r and emission direction $\mathbf{k} = \{k_r, k_z\}$ (ref. 6), $m = \hbar n/c\lambda_{co}$ is the photon mass, λ_{co} is the ground-state cavity cut-off wavelength, k_r is the transverse wavevector, $\Omega = (c/n)/\sqrt{\bar{L}\rho}$

https://doi.org/10.1038/s41566-024-01491-2

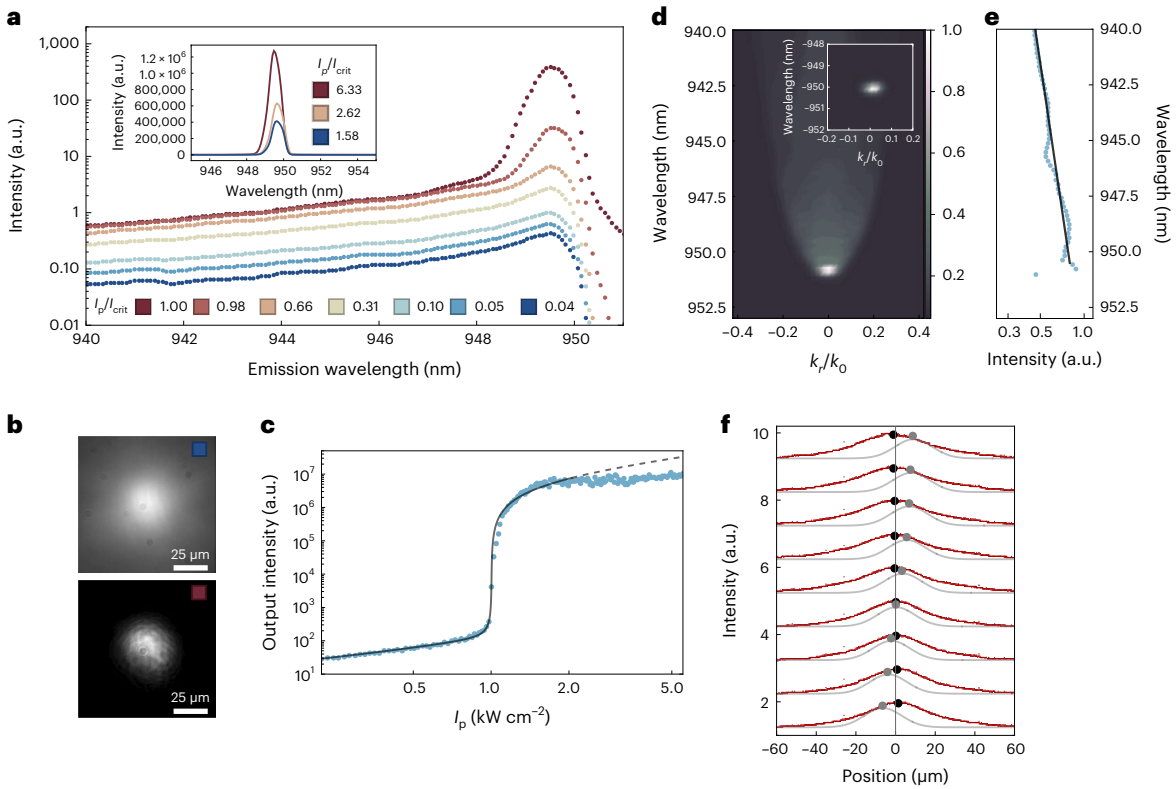

Fig. 2 | Thermalization and condensation of light in the semiconductor quantum well microcavity. a, Emission near the critical excitation intensity I_{crit} for a cavity tuned to $\lambda_{co} \approx 950$ nm. The inset shows the spectra above I_{crit} in the linear scale. **b**, Images of the thermal cloud for $I_p < I_{crit}$ (top) and the condensate for $I_p > I_{crit}$ (bottom). **c**, Condensate intensity as a function of excitation intensity. Condensate intensity is found by integrating the data in **a** at around $\lambda_{co} = \pm 1$ nm. Data are fitted to a semiconductor laser model (Supplementary Information). Deviation from linear behaviours at high excitation intensity is consistent with heating of the sample. **d**, Spectra as a function of in-plane momentum for the thermal cloud at $I_p = 0.2I_{crit}$. The inset shows the same for the BEC at $I_p = 2I_{crit}$. **e**, Data points are the summed intensity as a function of wavelength from **d**. Fitting the emission with a Bose–Einstein distribution (black line) gives a thermal cloud temperature of $T = 300 \pm 30$ K. **f**, Plot showing the spatial intensity of the thermal cloud (red) as the excitation beam position (grey) is varied.

is the transverse cavity trapping frequency, n is the average cavity refractive index and n_2 is the nonlinear refractive index. The final term accounts for photon–photon interactions due to nonlinear refraction, where $I(r)$ is the intracavity spatial intensity distribution.

The absorption of inorganic semiconductors is controlled using heterostructures, that is, regions of the crystal where the bandgap is varied via composition. Here we use a single InGaAs quantum well (Methods) with absorption peak wavelength $\lambda_{qw} = 930$ nm, which is far from the band edge absorption of the GaAs substrate at 875 nm. The quantum well sample without a commercial mirror was initially characterized by optical excitation with a continuous 785-nm-wavelength laser to find the emission and absorption spectra (Fig. 1b). Intraband carrier–phonon scattering on 10^{-13} s timescales ensures that carriers maintain a thermal distribution, and therefore, the absorption exhibits a characteristic Urbach tail, emulated also by a long-wavelength photoluminescence spectral tail.

It is well known that the ratio of absorption and emission spectra in semiconductors at thermal equilibrium follows the van Roosbroeck–Shockley (vRS) relation[4,25], analogous to the Kennard–Stepanov relation for organic materials[26]. Figure 1b compares the measured absorption spectrum from the semiconductor half-cavity with its predicted absorption spectrum, calculated from the measured photoluminescence spectrum using the vRS relation. We observe correspondence between these two datasets when the DBR loss $(1 - R_f)$ is added, which reveals good thermalization of electrons and phonons for $\lambda > 935$ nm. Around the bandgap, the vRS relation breaks down due to bound exciton absorption, which causes the absorption peak at 930 nm (refs. 27–29) (Supplementary Information provides a discussion of contributions to quantum well absorption). At room temperature, excitons in III–V semiconductors are weakly bound and dissociate into free electrons and holes on picosecond timescales[27], compared with the typical nanosecond radiative lifetime of the quantum well. As such, they do not meaningfully contribute to the emission spectrum of the quantum well, which is predominantly from the electronic continuum. A Gaussian function models the exciton absorption and reveals the correspondence between vRS and measured absorption across the whole spectral range (Fig. 1b). The spectra confirm that for $\lambda > 935$ nm, carriers and phonons in the quantum well are in thermal equilibrium, a prerequisite for photon condensation[30]. Thermal equilibrium breaks down near the exciton absorption in this III–V system, but could be sustained either under cryogenic conditions or for materials with stable excitons at room temperature. Thermalization is also possible when blue-detuned from the exciton peak, namely, $\lambda_{co} < 925$ nm, which has been confirmed in recent work[20].

Semiconductor lasers often use multiple quantum wells to increase the gain and power. Here only a single quantum well is necessary to produce a balance of cavity absorption α and mirror loss κ (ref. 31). Figure 1b shows that the single quantum well provides a peak of ~1.5% round-trip loss[32]. Meanwhile, the round-trip mirror loss, $1 - R_iR_b$, is smaller than 5×10^{-4} (Fig. 1b, horizontal line). The thermalization parameter $\gamma = \alpha/\kappa$ characterizes the extent of thermalization, with photon condensation expected to be optimal in the range of $0.1 < \gamma < 10.0$ (refs. 16,33). Here γ must be large enough for condensation to occur, but not so large that it increases the critical intensity. Here this interval lies in the long-wavelength Urbach tail of the quantum well absorption between $935 < \lambda_{co} < 960$ nm. We have, thus, designed the semiconductor mirror's central wavelength, $\lambda_{dbr} = 950$ nm, to overlap

https://doi.org/10.1038/s41566-024-01491-2

with this region. Since increasing the number of quantum wells would shift the range of good thermalization to regions where photoluminescence is weaker, it is preferable to use a single quantum well instead of the multiple wells employed in conventional semiconductor lasers.

Consider now the condensation mechanism for light interacting with a semiconductor quantum well in a microcavity. Figure 1c shows the electronic energy spectrum E_{el} as a function of in-plane electron momentum, $k_{e,r}$, (right) and density of electronic states, g_{qw}, (left), under optical excitation. Electron and hole populations are governed by Fermi–Dirac occupancy factors, namely, f_c and $1-f_v$, respectively (Methods). Their positions are set by quasi-Fermi levels for electrons ($E_{f,c}(N)$) and holes ($E_{f,v}(N)$), and controlled by the density of optically excited carriers N. The net rate of photon production at energy E_{ph} is set by a detailed balance of mode loss ($\kappa s(E_{ph}, N)$), net absorption ($\alpha(f_v - f_c)s(E_{ph}, N)$) and spontaneous emission ($\alpha f_c(1-f_v)$), where $s(E_{ph}, N)$ is the photon number. With good photon thermalization, $\gamma = \alpha/\kappa > 1$, the photon emission spectrum follows a Bose–Einstein distribution (Methods):

$$s(E_{ph}, N) \approx \frac{g_{ph}}{e^{(E_{ph}-\mu(N))/k_B T} - 1}, \quad (2)$$

where the photon chemical potential $\mu(N) = E_{f,c}(N) - E_{f,v}(N)$ is the difference between the electronic quasi-Fermi levels[3,5,19,20]. Figure 1d illustrates the photon energy spectrum as a function of k_r (right) with linear two-dimensional density of states g_{ph} and occupancy set by the Bose–Einstein factor f_{ph}. Photon thermalization follows naturally from the relationship between the Fermi–Dirac and Bose–Einstein occupancy factors, that is, $f_c(1-f_v) = f_{ph}(f_v - f_c)$. As shown in Fig. 1b, photon thermalization is expected to occur deep into the semiconductor's Urbach tail, below the quantum well band edge, where $E_{ph} < E_{qw} = hc/\lambda_{qw}$. For increasing carrier density, we would expect the chemical potential to increase, until it reaches the cavity ground-state energy, namely, $\mu \simeq E_{co} = hc/\lambda_{co}$, where photon condensation would be expected.

Figure 2a shows the emission spectra from the microcavity where the cut-off wavelength for longitudinal mode order $q = 9$ is set to $\lambda_{co} = 950$ nm, corresponding to $E_{co} \approx E_{qw} - 1.5k_B T$. At low pump intensity, we observe a Maxwell–Boltzmann distribution, which is indicative of thermalized photons according to equation (2)[7]. As the pump intensity I_p increases, emission near λ_{co} grows faster than the thermal tail, until the critical intensity I_{crit} is reached. At this point, the ground-state population becomes dominant, confirmed also by the spatial distribution of light (Fig. 2b). We observe the saturation of the thermal tail with increasing ground-state population. Figure 2a (inset) shows the increase in population of the lowest-energy state with intensities above $I_{crit} = 1\,\mathrm{kW\,cm^{-2}}$ (Supplementary Information). Above the critical pump intensity, the condensate's output is stable but deviates from a linear response due to heating (Fig. 2c).

The build up of coherence is a characteristic of BEC and so we also measured the first-order coherence time of the emitted light using a Michelson interferometer (Supplementary Information). The coherence time increases to >500 ps, which is >10κ. The coherence variation with power matches previous experimental measurements on dye-based photon BECs[34] and recent theoretical studies[35,36]. We also find that although the thermal cloud is unpolarized, the BEC is polarized with the pump beam, again following the behaviour shown by dye-based photon BECs[37,38]. The device is relatively efficient, emitting ~300 μW for an input power of 50 mW. The condensation is continuously sustained and remains stable under a range of cut-off wavelengths and pump conditions.

Figure 2d explores the thermalization and condensation in more detail using the momentum–space emission spectrum of the thermal cloud at $I_p = 0.2I_{crit}$. Here we reduced the mirror radius of curvature to 0.1 m to improve the collection of higher-energy photons from larger radial positions[39]. We observe a filled parabola as predicted by equation (1). Since the cavity dispersion is a function of both k_r and r, high-energy photons can occupy low k_r at high r. Fitting these spectra with a Bose–Einstein distribution gives a thermal cloud temperature of $T = 300 \pm 30$ K (ref. 7) (Supplementary Information), confirming a thermalized photon gas below the critical intensity. For comparison with the BEC state, Fig. 2d (inset) shows a measurement at $I_p = 2I_{crit}$, where the condensate is visible near $k_r = 0$.

We have also varied the position of the excitation beam relative to the optical axis (Fig. 2f). The thermal cloud does not shift in position from the cavity's energetic minimum, confirming good spatial thermalization[6,19]. By monitoring the thermal cloud size as a function of varying pump beam diameters, we have also explored spatial thermalization in more detail (Supplementary Information). We find that the thermal cloud saturates to a size corresponding to a temperature of $T = 300$ K within error, again confirming thermalization[40,41].

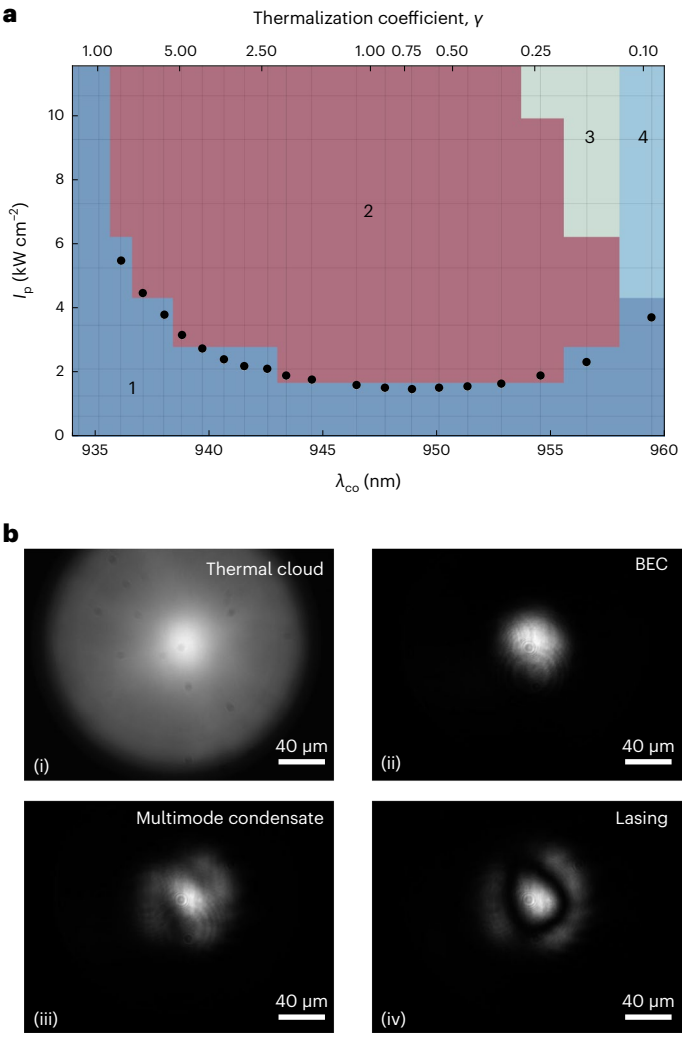

Fig. 3 | Phase diagram for the semiconductor quantum well microcavity. **a**, Phase diagram characterizing the spatial emission distribution as a function of cavity cut-off wavelength λ_{co} and excitation intensity. Data points indicate the critical excitation intensity I_{crit} extracted from the spectral data (Fig. 2b shows the methodology). The coloured areas represent the unique regions identified by using a clustering algorithm on images of the emission distributions taken at the values indicated by the intersecting horizontal and vertical lines. The clustering algorithm is fed an unsorted list of images that are subsequently assigned to groups. Four regions are identified: uncondensed/thermal cloud; photon condensate; break down of single-mode condensation; and higher-order mode condensation[16]. Images and details are available in the Supplementary Information. **b**, Example images from the four regions identified in **a**.

https://doi.org/10.1038/s41566-024-01491-2

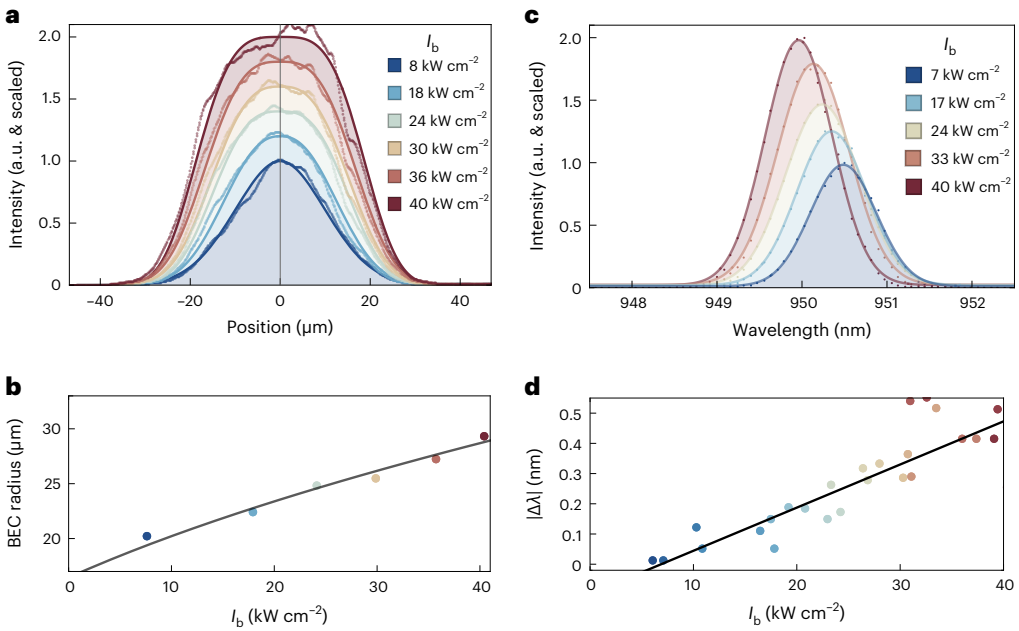

Fig. 4 | Interactions within the BEC. a, Radial intensity profiles of the BEC at λ_{co} = 950 nm for increasing intracavity condensate intensity I_b values. Data (points) are taken at the intensities from horizontal slices through images used in Fig. 3a, normalized and scaled to show change with I_b. To determine condensate radius r, data are fit with super-Gaussian curves (line). Size increase is attributed to repulsive interactions within the condensate. **b**, Condensate radius as a function of I_b (points). Data are fit to find n_2, using equation (6). **c**, Spectra of the BEC at λ_{co} = 950 nm for increasing I_b values, normalized and scaled. The central wavelengths are found by fitting spectra with Gaussians. BEC shifts to higher energy and lower wavelength due to repulsive interactions. **d**, BEC wavelength blueshifts as a function of I_b. Data are fit to find n_2, using equation (7).

Condensation occurs above the critical pump intensity, $I_{crit}(\lambda_{co})$, which depends on the cut-off wavelength (Fig. 3a). For operation nearer to the peak absorption λ_{qw}, a higher critical pump intensity is necessary as the quantum well absorption is larger and $\mu(N)$ must be increased closer to electronic inversion. We do not consider condensation for $\lambda_{co} < 935$ nm, where exciton absorption causes the vRS relation to break down. For increasing λ_{co}, cavity loss eventually exceeds absorption where photon thermalization is also expected to break down. It is still possible to observe critical behaviour, but with a higher threshold that suggests a larger value of $\mu(N)$ than would be necessary to observe condensation. This indicates the beginning of the laser regime.

To explore the photon condensation regime in more detail, we studied the spatial distribution of the condensed state as a function of λ_{co} and excitation intensity. Photon condensation should exhibit a signature of robust ground-state occupation. The phase diagram in Fig. 3a categorizes the types of spatial emission pattern, from the examples shown in Fig. 3b. Supplementary Information shows the full set of condensate distribution images.

Below the critical excitation intensity, a thermal cloud is observed for all the cut-off wavelengths; an example is shown in Fig. 3b(i). Above the critical pump intensity and for $936 < \lambda_{co} < 957$ nm, condensation in the lowest-energy cavity mode is observed (Fig. 3b(ii)). Meanwhile, for $\lambda_{co} \geq 957$ nm, a higher-order mode (Fig. 3b(iv)) occurs at the critical intensity, suggesting laser operation. The presence of lasing here, rather than condensation, can be explained by the decrease in γ below the value of 0.1; there is insufficient absorption to allow the system to thermalize before light is lost from the cavity[16,31]. As the photons cannot reach thermal equilibrium, BEC cannot occur; instead, above I_{crit}, lasing occurs. Of particular interest is the behaviour at λ_{co} = 956.5 nm, where condensation occurs just above I_{crit}, but as the pump intensity is increased further, a multimode distribution (Fig. 3b(iii)) is observed. This is consistent with the expected phases of photon BEC from both simulation[16] and measurement on dye-based condensates[33].

Interactions in photon condensates are mediated through refractive index variations due to free-carrier effects, heating or the Kerr effect, leading to relatively small dimensionless interaction parameters, that is, $\tilde{g} \leq 10^{-4}$ (refs. 6,42). For dye-based condensates, nonlinear refraction is associated with heating of the dye and has an overall repulsive effect where dn/dT is negative, that is, the refractive index, effective cavity length and cut-off wavelength are reduced with heating. Evidence of device heating is clearly seen in the saturation of light output versus pump response (Fig. 2c). However, dn/dT is positive in GaAs (refs. 43,44), and therefore, heating would have an attractive influence on the condensate.

As the intracavity condensate intensity I_b increases, we see an increase in the size of the condensate (Fig. 4a). This is a repulsive effect that requires a negative refractive index change, attributable to variations in the excited carrier density N, where dn/dN is negative for InGaAs quantum wells[45,46]. Supplementary Information discusses distinguishing the influences of excitation beam and condensate intensities on refractive index changes. Relating the observed increase in condensate radius to I_b (Fig. 4b), we compute a dimensionless interaction parameter $\tilde{g} = 0.0025 \pm 0.0004$ (Methods). Evidence of repulsive interactions can also be seen in the wavelength of the BEC (Fig. 3c), which shifts to higher energy as I_b increases. Using the energy shift, we compute a dimensionless interaction parameter of $\tilde{g} = 0.0022 \pm 0.0004$.

These values are higher than those reported for dye-based condensates[6,42], despite the measured effect also being opposed by the effect of heating. The excited dense electron–hole plasma within the semiconductor must be the origin of the observed photon interaction, but the exact mechanism(s) (for example, carrier dispersion, inhomgeneity, bandgap renormalization and timescales) here require further research before explicit comparison with other condensates of light can be drawn. The interaction strength could be increased by mitigating heating, either by increasing the excitation beam size or the excitation wavelength, reducing the longitudinal mode order or increasing the number of quantum wells.

This work provides a robust new physical system for investigating photon BEC, through the use of an inorganic semiconductor quantum well in an open microcavity. Unlike monolithic cavities, we directly vary the cavity length to control the system's ability to thermalize, thereby identifying the boundary between photon BEC and lasing. We also see low I_{crit} values within the condensate regime, due to operation below electronic inversion in the quantum well's Urbach tail[14]. Combined with the inherent ground-state operation and control of spatial trapping, condensation in semiconductor open microcavities could allow for the design of efficient and large-mode-area coherent light sources.

Although organic-dye-based photon BECs have been instrumental in the foundation of the field, photon BECs in semiconductor environments overcome fundamental limitations of dye- and exciton-based systems. The continuous operation enabled by semiconductors is key for practical applications, and the strong interaction between photons observed in this work enable fundamental experiments that currently seem elusive in dye-based experiments. Semiconductor setups promise access to superfluidity of light[42,47]; combined with the ability to sustain the condensate indefinitely, vortex formation[48] could be investigated. The use of spatially shaped potentials[49] with the available interaction strengths here would allow the Josephson effect to be achieved between photon BECs[50,51], opening the role of thermalized light in quantum technology applications under ambient conditions.

Online content

Any methods, additional references, Nature Portfolio reporting summaries, source data, extended data, supplementary information, acknowledgements, peer review information; details of author contributions and competing interests; and statements of data and code availability are available at https://doi.org/10.1038/s41566-024-01491-2.

References

1. Hall, R. N., Fenner, G. E., Kingsley, J. D., Soltys, T. J. & Carlson, R. O. Coherent light emission from GaAs junctions. *Phys. Rev. Lett.* **9**, 366–368 (1962).
2. Nathan, M. I., Dumke, W. P., Burns, G., Dill, F. H. & Lasher, G. Stimulated emission of radiation from GaAs p-n junctions. *Appl. Phys. Lett.* **1**, 62–64 (1962).
3. Bernard, M. G. A. & Duraffourg, G. Laser conditions in semiconductors. *Phys. Stat. Sol. (b)* **1**, 699–703 (1961).
4. van Roosbroeck, W. & Shockley, W. Photon-radiative recombination of electrons and holes in germanium. *Phys. Rev.* **94**, 1558–1560 (1954).
5. Wurfel, P. The chemical potential of radiation. *J. Phys. C: Solid State Phys.* **15**, 3967–3985 (1982).
6. Klaers, J., Vewinger, F. & Weitz, M. Thermalization of a two-dimensional photonic gas in a 'white wall' photon box. *Nat. Phys.* **6**, 512–515 (2010).
7. Klaers, J., Schmitt, J., Vewinger, F. & Weitz, M. Bose-Einstein condensation of photons in an optical microcavity. *Nature* **468**, 545–548 (2010).
8. Davis, K. B. et al. Bose-Einstein condensation in a gas of sodium atoms. *Phys. Rev. Lett.* **75**, 3969–3973 (1995).
9. Anderson, M. H., Ensher, J. R., Matthews, M. R., Wieman, C. E. & Cornell, E. A. Observation of Bose-Einstein condensation in a dilute atomic vapor. *Science* **269**, 198–201 (1995).
10. Demokritov, S. O. et al. Bose-Einstein condensation of quasi-equilibrium magnons at room temperature under pumping. *Nature* **443**, 430–433 (2006).
11. High, A. A. et al. Spontaneous coherence in a cold exciton gas. *Nature* **483**, 584–588 (2012).
12. Hakala, T. K. et al. Bose-Einstein condensation in a plasmonic lattice. *Nat. Phys.* **14**, 739–744 (2018).
13. Deng, H., Weihs, G., Santori, C., Bloch, J. & Yamamoto, Y. Condensation of semiconductor microcavity exciton polaritons. *Science* **298**, 199–202 (2002).
14. Bloch, J., Carusotto, I. & Wouters, M. Non-equilibrium Bose-Einstein condensation in photonic systems. *Nat. Rev. Phys.* **4**, 470–488 (2022).
15. Chen, C. C. et al. Continuous Bose-Einstein condensation. *Nature* **606**, 683–687 (2022).
16. Hesten, H. J., Nyman, R. A. & Mintert, F. Decondensation in nonequilibrium photonic condensates: when less is more. *Phys. Rev. Lett.* **120**, 040601 (2018).
17. Barland, S., Azam, P., Lippi, G. L., Nyman, R. A. & Kaiser, R. Photon thermalization and a condensation phase transition in an electrically pumped semiconductor microresonator. *Opt. Express* **29**, 8368–8375 (2021).
18. Bajoni, D., Senellart, P., Lemaître, A. & Bloch, J. Photon lasing in GaAs microcavity: similarities with a polariton condensate. *Phys. Rev. B* **76**, 201305 (2007).
19. Loirette-Pelous, A. & Greffet, J. J. Photon Bose-Einstein condensation and lasing in semiconductor cavities. *Laser Photon. Rev.* **17**, 2300366 (2023).
20. Pieczarka, M. et al. Bose–Einstein condensation of photons in a vertical-cavity surface-emitting laser. *Nat. Photon.* https://doi.org/10.1038/s41566-024-01478-z (2024).
21. Kasprzak, J. et al. Bose-Einstein condensation of exciton polaritons. *Nature* **443**, 409–414 (2006).
22. Balili, R., Hartwell, V., Snoke, D., Pfeiffer, L. & West, K. Bose-Einstein condensation of microcavity polaritons in a trap. *Science* **316**, 1007–1010 (2007).
23. Deng, H., Weihs, G., Snoke, D., Bloch, J. & Yamamoto, Y. Polariton lasing vs. photon lasing in a semiconductor microcavity. *Proc. Natl Acad. Sci. USA* **100**, 15318–15323 (2003).
24. Pieczarka, M. et al. Crossover from exciton-polariton condensation to photon lasing in an optical trap. *Opt. Express* **30**, 17070–17079 (2022).
25. Bhattacharya, R., Pal, B. & Bansal, B. On conversion of luminescence into absorption and the van Roosbroeck-Shockley relation. *Appl. Phys. Lett.* **100**, 222103 (2012).
26. Kennard, E. H. On the thermodynamics of fluorescence. *Phys. Rev.* **11**, 29–38 (1918).
27. Chemla, D., Miller, D., Smith, P., Gossard, A. & Wiegmann, W. Room temperature excitonic nonlinear absorption and refraction in GaAs/AlGaAs multiple quantum well structures. *IEEE J. Quantum Electron.* **20**, 265–275 (1984).
28. Yoshita, M., Kamide, K., Suzuura, H. & Akiyama, H. Applicability of continuum absorption in semiconductor quantum wells to absolute absorption-strength standards. *Appl. Phys. Lett.* **101**, 032108 (2012).
29. Bhattacharya, R. et al. Measurements of the electric field of zero-point optical phonons in GaAs quantum wells support the Urbach rule for zero-temperature lifetime broadening. *Phys. Rev. Lett.* **114**, 047402 (2015).
30. Kirton, P. & Keeling, J. Nonequilibrium model of photon condensation. *Phys. Rev. Lett.* **111**, 100404 (2013).
31. Kirton, P. & Keeling, J. Thermalization and breakdown of thermalization in photon condensates. *Phys. Rev. A* **91**, 033826 (2015).
32. Fang, H. et al. Quantum of optical absorption in two-dimensional semiconductors. *Proc. Natl Acad. Sci. USA* **110**, 11688–11691 (2013).
33. Rodrigues, J. D. et al. Learning the fuzzy phases of small photonic condensates. *Phys. Rev. Lett.* **126**, 150602 (2021).
34. Walker, B. T. et al. Driven-dissipative non-equilibrium Bose-Einstein condensation of less than ten photons. *Nat. Phys.* **14**, 1173–1177 (2018).
35. Tang, Y., Dhar, H. S., Oulton, R. F., Nyman, R. A. & Mintert, F. Breakdown of temporal coherence in photon condensates. *Phys. Rev. Lett.* **132**, 173601 (2024).

36. Tang, Y., Dhar, H. S., Oulton, R. F., Nyman, R. A. & Mintert, F. Photon-photon correlation of condensed light in a microcavity. *Phys. Rev. A* **109**, 043713 (2024).
37. Greveling, S., van der Laan, F., Jagers, H. C. & van Oosten, D. Polarization of a Bose-Einstein condensate of photons in a dye-filled microcavity. Preprint at https://arxiv.org/abs/1712.08426 (2017).
38. Moodie, R. I., Kirton, P. & Keeling, J. Polarization dynamics in a photon Bose-Einstein condensate. *Phys. Rev. A* **96**, 043844 (2017).
39. Greveling, S., Perrier, K. L. & van Oosten, D. Density distribution of a Bose-Einstein condensate of photons in a dye-filled microcavity. *Phys. Rev. A* **98**, 013810 (2018).
40. Marelic, J. & Nyman, R. A. Experimental evidence for inhomogeneous pumping and energy-dependent effects in photon Bose-Einstein condensation. *Phys. Rev. A* **91**, 033813 (2015).
41. Keeling, J. & Kirton, P. Spatial dynamics, thermalization, and gain clamping in a photon condensate. *Phys. Rev. A* **93**, 013829 (2016).
42. Marelic, J., Walker, B. T. & Nyman, R. A. Phase-space views into dye-microcavity thermalized and condensed photons. *Phys. Rev. A* **94**, 063812 (2016).
43. Talghader, J. & Smith, J. S. Thermal dependence of the refractive index of GaAs and AlAs measured using semiconductor multilayer optical cavities. *Appl. Phys. Lett.* **66**, 335–337 (1995); erratum **69**, 2608 (1996).
44. Skauli, T. et al. Improved dispersion relations for gaas and applications to nonlinear optics. *J. Appl. Phys.* **94**, 6447–6455 (2003).
45. Ehrlich, J., Neilson, D. & Walker, A. Carrier-dependent nonlinearities and modulation in an InGaAs SQW waveguide. *IEEE J. Quantum Electron.* **29**, 2319–2324 (1993).
46. Ehrlich, J., Neilson, D., Walker, A. & Hopkinson, M. Guided-wave measurements of real-excitation optical nonlinearities in a tensile strained InGaAs on InP quantum well at 1.5 μm. *Opt. Commun.* **102**, 473–477 (1993).
47. Alaeian, H., Schedensack, M., Bartels, C., Peterseim, D. & Weitz, M. Thermo-optical interactions in a dye-microcavity photon Bose-Einstein condensate. *New J. Phys.* **19**, 115009 (2017).
48. Dhar, H. S., Zuo, Z., Rodrigues, J. D., Nyman, R. A. & Mintert, F. Quest for vortices in photon condensates. *Phys. Rev. A* **104**, L031505 (2021).
49. Kurtscheid, C. et al. Thermally condensing photons into a coherently split state of light. *Science* **366**, 894–897 (2019).
50. Ryu, C., Blackburn, P. W., Blinova, A. A. & Boshier, M. G. Experimental realization of Josephson junctions for an atom SQUID. *Phys. Rev. Lett.* **111**, 205301 (2013).
51. Vretenar, M., Kassenberg, B., Bissesar, S., Toebes, C. & Klaers, J. Controllable Josephson junction for photon Bose-Einstein condensates. *Phys. Rev. Research* **3**, 023167 (2021).

Methods

Sample preparation

The samples were grown by molecular-beam epitaxy on two-inch semi-insulating double-side-polished gallium arsenide (GaAs(001)) substrates on a DCA P700 MBE system. Following oxide removal, a 300 nm GaAs buffer layer and 32.5-pair GaAs(67.4 nm)/AlAs(80.1 nm) DBR stack and lower 126.8 nm of the GaAs cavity region were grown at 590 °C before the substrate temperature was reduced to 480 °C for the deposition of the 8 nm $In_{0.1}Ga_{0.9}As$ quantum well and 20 nm GaAs capping layer. Substrate temperatures were measured using kSA BandiT band edge thermometry[52]. The temperature was then raised to 590 °C for completion of the structure with 32.6 nm GaAs and then a 5.0 nm AlAs window layer to limit surface recombination[53] and 5.0 nm GaAs cap. The optimal growth temperature for the InGaAs quantum well was determined by measuring the room-temperature photoluminescence intensity in a series of calibration samples without a DBR. The presence of the 5 nm AlAs window layer was critical for obtaining strong luminescence from this near-surface quantum well, with the photoluminescence intensity being 100 times higher compared with a control sample with no window layer present.

Experimental setup

We assembled an open-access microcavity (Fig. 1a). The commercial mirror was cut down to a diameter of ≤1.4 mm, to allow the two halves of the microcavity to approach with a minimum separation of <1 µm at the optical axis. We adjusted the cavity length so that the longitudinal mode number was $q = 9$. The optical cavity length L is controlled via a piezo actuator, which is stabilized to the interference pattern of a secondary light-emitting diode light source. Here we used the image of interference rings from a reflected 840 nm laser diode (Thorlabs, LED840L) through a commercial mirror (LAYERTEC), measured on a camera (Blackfly, S BFS-U3-16S2M), to monitor the fluctuating cavity length. This is then used to drive a proportional–integral–derivative locking loop using a piezoelectric positioning stage (Thorlabs, NFL5DP20M) to lock the cavity length to within our spectrometer resolution.

We excite the quantum well using a 785 nm laser diode (Thorlabs, L785H1) focused through an objective lens (Mitutoyo, M Plan Apo NIR 20X) and the cut-down commercial mirror. The emission is collected through the substrate mirror using an objective lens (Mitutoyo, M Plan Apo NIR 50X) and split on a beamsplitter between a camera (Blackfly, S BFS-U3-16S2M) and spectrometer (AvaSpec, ULS2048L). Two-dimensional spectra are measured using an imaging spectrometer (Acton 300, Princeton Instruments) combined with a cooled charge-coupled device camera (PIXIS 100, Princeton Instruments). We filter the camera image using a 925 nm long-pass filter (Thorlabs) to remove bulk GaAs emission and pump light.

Detailed balance for a semiconductor quantum well in a microcavity

The net rate of photon production in the nth cavity mode for an excited carrier density N is set by a detailed balance of modal emission, absorption and cavity loss. The steady-state photon number rate equation can be written as $\alpha_n f_c(1-f_v) + \alpha_n(f_c - f_v)s_n = \kappa_n s_n$, where s_n is the photon number in mode n, $\alpha_n \approx \alpha$ is the modal absorption rate and $\kappa_n \approx \kappa$ is the modal cavity loss rate. $f_{c/v}^{-1} = \exp\{(E_{c/v}(k_e) - E_{f,c/v}(N))/k_B T\} + 1$ are the Fermi–Dirac probability functions, where $E_{c/v}(k_e)$ are the conduction/valence band energies at constant crystal momentum k_e, such that the photon energy $E_{ph} = E_c(k_e) - E_v(k_e)$, and $E_{f,c/v}(N)$ are the quasi-Fermi levels. We also identify the net modal material loss rate as $\alpha'(N) = \alpha(f_v - f_c)$, and the spontaneous emission rate $r_{sp} = \alpha f_c(1-f_v)$. Each mode can be identified with an emission energy E_{ph} through the dispersion relation (equation (1)) so that the modal photon numbers can be expressed as $s_n = s(E_{ph}, N)$. Then, the photon number spectrum may be written as

$$s(E_{ph}, N) = \frac{1}{e^{(E_{ph}-\mu(N))/k_B T} - 1 + \kappa/r_{sp}}, \tag{3}$$

where $(e^{(E_{ph}-\mu(N))/k_B T} - 1)f_c(1-f_v) = (f_v - f_c)$. This expression is expected for a driven-dissipative semiconductor BEC[19,20]. We can also express the spontaneous emission in terms of the net cavity loss rate $\alpha'(N)$ such that

$$s(E_{ph}, N) = \frac{1}{\left(e^{(E_{ph}-\mu(N))/k_B T} - 1\right)\left(1 + \frac{\kappa}{\alpha'(N)}\right)}. \tag{4}$$

Under low excitation, $f_v - f_c \approx 1$, and with good photon thermalization, $\alpha'(N) \approx \alpha$ and $\kappa/\alpha = \gamma^{-1} \ll 1$, the photon number in the nth mode follows a Bose–Einstein distribution with chemical potential $\mu(N) = E_{f,c}(N) - E_{f,v}(N)$. Under high excitation, a Bose–Einstein distribution is maintained provided $\alpha'(N) \gg \kappa$ (ref. 19). In the case where $\alpha'(N) \gg \kappa$ and accounting for the density of photon states g_{ph}, the total photon spectrum is

$$s(E_{ph}, N) \approx \frac{g_{ph}}{e^{(E_{ph}-\mu(N))/k_B T} - 1}. \tag{5}$$

Photon interaction

The dimensionless interaction parameter used to quantify interactions within a condensate can be expressed as $\tilde{g} = -(m_{ph}^4 c^6 n_2)/(2\pi\hbar q n)$ (refs. 7,54). We can relate the condensate radius r increase (Fig. 4a) to the nonlinear refractive index n_2 using equation (1). Here we fit super-Gaussians to the observed mode profiles. Although these are not solutions to the nonlinear Schrödinger equation, the fitting is close and allows us to accurately extract the e^{-2} beam width. Nonlinear refraction may occur due to the excitation beam and BEC, where additional analysis shows the BEC dominates (Supplementary Information). We thus take $I(r)$ as the BEC intensity $I_b(r)$, found through the measurement of the output power (Supplementary Information). We set the energy change from the increase in condensate size, from an initial size of r_{init}, according to $1/2 m_{ph}\Omega^2 r^2$ equal to the interaction term $-m_{ph}c^2 n_2/n^3 I_b$ and rearranging, we find

$$r = \sqrt{r_{init}^2 - \frac{2c^2 I_b n_2}{n^3 \Omega^2}}, \tag{6}$$

which we can fit to the measured condensate size. Here I_b is taken as the peak intensity, giving a lower bound interaction strength. From fitting, we also find $r_{init} = 17 \pm 1$ µm, matching the expected condensate size from the cavity geometry of 17 ± 1 µm. This indicates we are seeing condensation into the lowest-energy state of the system.

For the change in condensate wavelength, we can find the corresponding refractive index change $\Delta n = n_2 I_b$ through

$$\lambda = \lambda_{init} + \frac{n_2 \lambda_{init} I_b}{n}, \tag{7}$$

where λ_{init} is the wavelength at the phase change to BEC.

Data availability

Data used are available via Zenodo at https://doi.org/10.5281/zenodo.11370546 (ref. 55)

References

52. Farrer, I. et al. Substrate temperature measurement using a commercial band-edge detection system. *J. Cryst. Growth* **301–302**, 88–92 (2007).
53. Mir, Y., Amine, A., Bouabdellaoui, M., Zazi, K. & Zazoui, M. The window layers effect on the hardness improvement of space solar cells exposed to the 1MeV electron irradiations. *Opt. Quant. Electron.* **45**, 1189–1197 (2013).

54. Nyman, R. A. & Szymańska, M. H. Interactions in dye-microcavity photon condensates and the prospects for their observation. *Phys. Rev. A* **89**, 033844 (2014).
55. Schofield, R. C. et. al. Bose-Einstein condensation of light in a semiconductor quantum well microcavity. *Zenodo* https://doi.org/10.5281/zenodo.11370546 (2024).

Acknowledgements

We thank J. Murphey for his expert optical workshop support and O. Blaszczyk for his early contributions to the experimental apparatus and design. This work was supported by the UK Engineering and Physical Sciences Research Council project 'Near-equilibrium thermalised quantum light' (EP/S000755/1) (all authors) and by the EU Project 'Photons for Quantum Simulation' PhoQuS (AMD-820392-7) (H.S.D., R.M., F.M., R.A.N. and R.F.O.).

Author contributions

R.A.N. and R.F.O. conceptualized the work. E.C., I.F., A.T. and J.H. fabricated the semiconductor samples, which were designed and simulated by R.F.O. M.F. and R.A.N. designed and implemented the experimental setup. R.C.S., M.F. and T.S.M. performed the experimental measurements. R.C.S. performed the data analysis. R.C.S., M.F., H.S.D., R.M., F.M. and R.F.O. interpreted the results. R.C.S. drafted the manuscript and all authors contributed to the final draft. R.F.O. supervised the project.

Competing interests

The authors declare no competing interests.

Additional information

Supplementary information The online version contains supplementary material available at https://doi.org/10.1038/s41566-024-01491-2.

Correspondence and requests for materials should be addressed to Ross C. Schofield or Rupert F. Oulton.

Peer review information *Nature Photonics* thanks the anonymous reviewers for their contribution to the peer review of this work.